Photoemission studies of single crystal CuO(100)

1999 J. Phys.: Condens. Matter 11 5021

(http://iopscience.iop.org/0953-8984/11/26/306)

J. Phys.: Condens. Matter **11** (1999) 5021–5043. Printed in the UK PII: S0953-8984(99)01428-9

Photoemission studies of single crystal CuO(100)

S Warren†, W R Flavell†¶, A G Thomas†, J Hollingworth†, P L Wincott‡, A F Prime‡, S Downes§ and Changkang Chen‖

† Department of Physics, UMIST, PO Box 88, Manchester M60 1QD, UK
‡ IRCSS/Department of Chemistry, University of Manchester, Manchester M13 9PL, UK
§ CLRC Daresbury Laboratory, Daresbury, Warrington, Cheshire WA4 4AD, UK
‖ Clarendon Laboratory, University of Oxford, Oxford OX1 3PU, UK

E-mail: wendy.flavell@umist.ac.uk

Received 29 January 1999

Abstract. Photoemission studies of a cleaved CuO single crystal have been carried out, using station 6.2 at the CLRC Daresbury Laboratory. The (100) face orientation produced by anvil cleaving was determined using Laue back-reflection and LEED. Resonant photoemission measurements at the Cu 3p → Cu 3d threshold were undertaken and these are compared with existing data from oxidized copper films, and with theoretical configuration interaction calculations for the resonance process. Angle-resolved measurements of the valence band structure have also been performed at different photon energies along three crystal axes, and these are mapped onto the 3D structure of the monoclinic material. This allows general comparison with existing momentum-resolved calculations. The validity of comparisons with both localized and delocalized descriptions of the electronic structure of this highly correlated oxide is discussed.

1. Introduction

CuO is a grey–black p-type semiconductor [1] which crystallizes in the complex monoclinic tenorite structure with Cu–O planes along the $[1\bar{1}0]$ and [110] directions (figure 1 [1–3]). Although the local environment of Cu in these planes is strongly distorted, the planes are similar to those thought to be responsible for superconductivity in the layered cuprates. An understanding of the electronic structure of this oxide is therefore of importance in developing models for the normal state behaviour of superconducting cuprates.

Interest in the electronic structure of CuO has meant that there have been several calculated descriptions of the DOS/JDOS function, both from a localized cluster standpoint (e.g. configuration interaction (CI) calculation [4–6]), and attempts at delocalized (band) descriptions, based on the local-density-functional approximation (LDA) [7]. More recently, attempts have been made to improve on the LDA calculation, by a more explicit inclusion of electron correlation effects, using the self-interaction-corrected local-spin-density (SIC−LSD) formalism, LSD + U methods [8] and tight-binding Hartree–Fock calculation [9], all making use of the Igarashi three-particle approximation for the treatment of many-body effects [10, 11]. All approaches are to some extent hampered by the complex CuO structure; CI calculations approximate the highly distorted C_{2h} local point symmetry around Cu to D_{4h} [4–6], while there are very few band structure calculations which use the full tenorite structure [7, 9], rather than approximating it to cubic rock salt.

¶ Corresponding author.

0953-8984/99/265021+23$19.50

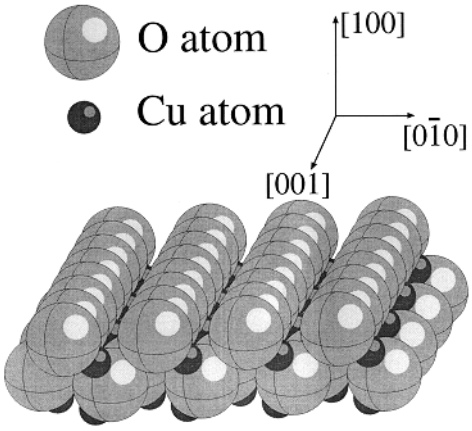

(a)

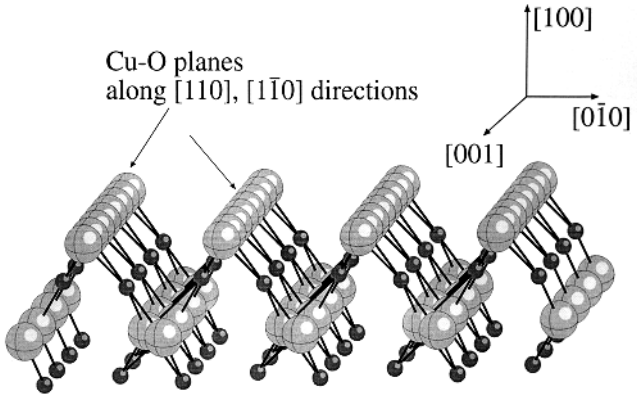

(b)

Figure 1. (a) The crystal structure of CuO using the lattice parameters from [1] and [2]. The diagram shows the (100) face, assuming an oxygen plane termination. The size of the copper and oxygen species reflects the ionic radii of [3]. (b) A projection of the crystal structure of CuO showing the inclination of the Cu–O planes to the (100) surface.

Photoemission is a powerful experimental probe of electronic structure which should allow us to determine which model is the most appropriate starting point for treating this oxide. Resonant photoemission allows the atomic character of the JDOS probed in the experiment to be determined, while, in principle, angle-resolved photoemission from single crystal samples gives information on dispersions of the spectral profile which may be compared with momentum-resolved calculations.

In the case of CuO, a number of resonant photoemission experiments have been carried out on polycrystalline oxidized films of Cu and composite single crystals [4, 5, 12–14]. In addition to the main valence band feature, these have revealed the presence of a higher binding energy 'satellite' feature, and led to assignment of these features as due to $d^9\underline{L}^1$ and d^8 final states respectively (where $\underline{L}$ denotes a ligand oxygen hole). The positions of these features on a binding energy scale will depend on the relative size of the *d–d* Coulomb interaction (U_d) and the charge transfer energy (Δ_{pd}). For CuO Δ_{pd} is lower than U_d with the result

that CuO is predicted to be a charge-transfer type semiconductor. CI predictions based on these parameters [4–6] agree well with experimental Cu 3p resonant photoemission from polycrystalline samples [5, 13], and reproduce the observed satellite feature. Here, these spectra are compared with those recorded from an oriented single crystal of CuO. In particular, a discrepancy in the reported resonance behaviour [5, 12] of one of the satellite features in the spectrum is examined.

The reproduction of the satellite feature in CI calculations is in itself an indication of strong electron correlation in this material, and a testament to the success of a localized starting point. Rather fewer calculations have been made using delocalized band approaches such as LDA (and of these, very few are performed within the monoclinic tenorite structure [7]). In contrast to CI calculations, the neglect of explicit electron correlation effects means that local-density theory band structure calculations cannot reproduce the satellite features, and also predict a metallic ground state for semiconducting CuO. Some improvements are possible in LSD + U and SIC approaches [8], but the energy and intensity of the satellite features are not well reproduced. A slightly more satisfactory result has been achieved in TBHF calculations including a local three-body scattering approximation (TBHF + Σ) [9]. The momentum dependence of the spectral function has also been calculated along several symmetry axes, allowing comparison with angle-resolved photoemission experiments [9].

Previous work on CuO has used polycrystalline thin film or composite single crystal specimens [4, 5, 12–14], so precluding angle-resolved work. Here we present angle-resolved spectra recorded from an oriented single crystal of CuO. In an initial brief communication, we presented spectra recorded along one azimuth [15], approximating to the ΓA direction. Here we present a more complete data set, including spectra recorded along further azimuths (one of which approximates to ΓY), and normal emission spectra recorded as a function of photon energy (approximating to ΓX). These new data enable us to make direct contact with the momentum-resolved spectral functions calculated by Takahashi and Igarashi for the ΓX and ΓY directions [9]. Comparison with LDA calculations is also considered. In addition, a detailed comparison of CI-calculated [5] and experimental Cu 3p resonant photoemission from the (100) surface is presented. We discuss the extent to which each theoretical picture provides an adequate description of the observed spectra.

2. Experiment

These experiments were performed on beamline 6.2 at the Synchrotron Radiation Source, CLRC Daresbury Laboratory, using the toroidal grating monochromator ($15 \leqslant h\nu \leqslant 90$ eV). A VG ADES 400 electron analyser, with a fixed entrance aperture angular acceptance of $\pm 2^\circ$, was used and the experimental resolution (combined monochromator and analyser resolution) was 0.16 eV. A large single crystal of CuO grown by the flux method [16] was supplied by the UK National Crystal Growth Centre for Superconducting Oxides. This was aligned and the orientation determined using Laue back-reflection. A detailed comparison of the patterns obtained from the crystal, and simulated Laue patterns (generated by LAUEGEN software at Daresbury Laboratory) was required to determine the orientation. The simulated pattern for the (100)-oriented face and the experimental Laue pattern are shown in figure 2. The CuO crystal was then cleaved parallel to the (100) face at room temperature in UHV using a VSW anvil crystal cleaver. After the photoemission measurements had been completed, a LEED pattern of the face under examination was also recorded. An example is shown in figure 3. This is a simple rectangular pattern and the ratio of the lengths in the LEED pattern is consistent with the ratio b^*/c^* expected for the (100) face. No additional spots are observed, and this confirms that the face examined was unreconstructed CuO(100).

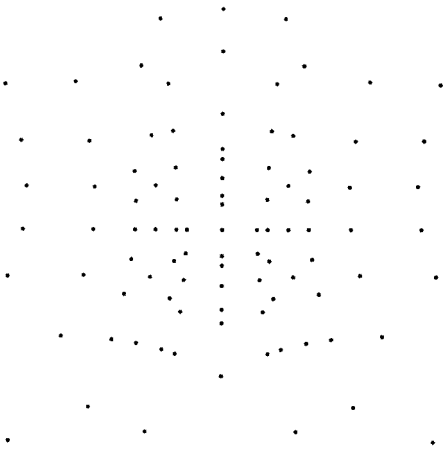

(a)

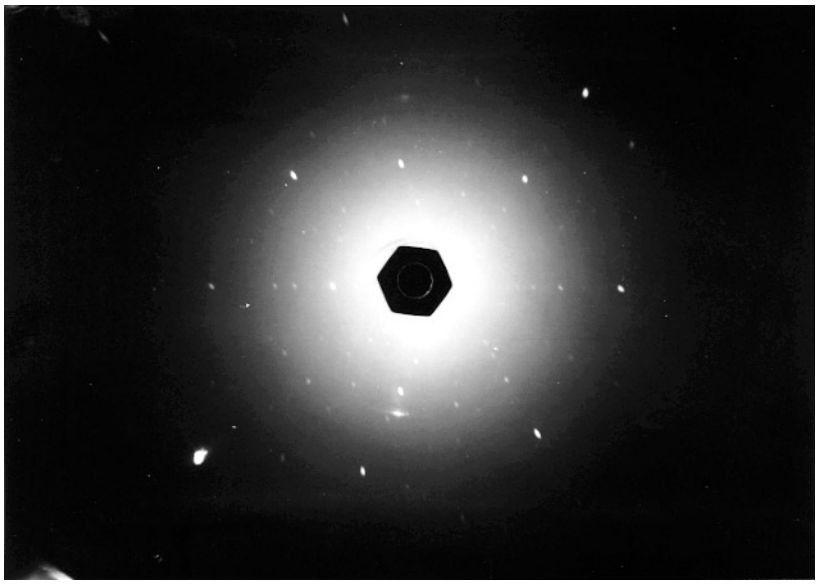

(b)

Figure 2. (a) The Laue pattern of CuO(100) simulated using the LAUEGEN software at Daresbury Laboratory; (b) the pattern recorded for the cleaved face examined in the photoemission experiments.

The Fermi edge position was determined by measurements from the metallic sample holder. The workfunction was determined as 4.75 eV from measurements of the secondary electron background cutoff from a biased sample. The base pressure was 3.5×10^{-11} mbar, and sample cleanliness was monitored by observation of features on the high binding energy side of the valence band where changes have been reported as the surface degrades [12]. No detectable increase in surface contaminants was observed over a period of several days, suggesting that the CuO(100) surface produced was very stable towards degradation under the conditions of the experiment.

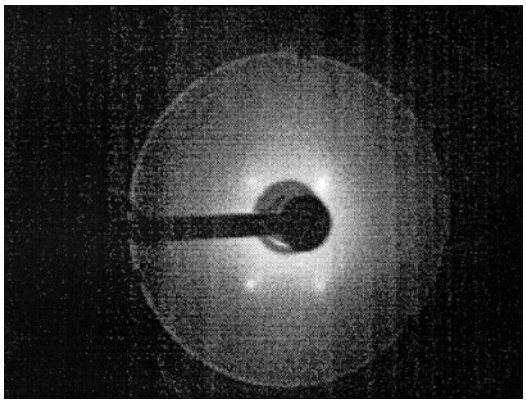

Figure 3. The LEED pattern obtained from a cleaved CuO crystal, recorded at an electron beam energy of 179 eV. The pattern aspect ratio is consistent with the ratio b^*/c^*.

3. Results and discussion

We consider first angle-resolved photoemission data (section 3.1), making general comments (section 3.1.1), followed by a more explicit comparison of data recorded along the [001] and [010] azimuths, and in normal emission, with momentum-resolved calculations (sections 3.1.2–3.1.4). In section 3.2, we discuss resonant photoemission data, again beginning with general comments (section 3.2.1), followed by a direct comparison with calculated resonance profiles (section 3.2.2).

3.1. Angle-resolved photoemission; comparison with momentum-resolved calculation

3.1.1. General comparison. Valence band data have been recorded over a range of polar and azimuthal angles and using different photon energies. Overall, the spectral profiles are in good general agreement with earlier data from polycrystalline thin film or composite single crystal specimens [4, 5, 12–14]. Ignoring for the present the satellite structure below 9 eV binding energy, we find that the overall features of the main valence band structure (for example those seen in figure 4(a)) show moderate agreement with those predicted by LDA calculation [7]: both have approximately the same width (8 eV for the experimental spectrum, and 9 eV for the theoretical data); the valence band maximum position lies at the same value of 3 eV, with little dispersion on tracking through the Brillouin zone; while features to the high binding energy side of the valence band maximum (5–8 eV) show slightly more substantial dispersion as predicted (see e.g. figure 4(c), discussed further below). There are, however, notable discrepancies. The LDA calculations falsely predict crossings of the Fermi level [7, 9], with marked dispersion of the states close to E_F (particularly along ΓA, ΓX and ΓY), whereas CuO is semiconducting. We have examined the feature closest to the Fermi energy (in the binding energy range 0.5–1.5 eV) in some detail, but have found no discernible dispersion at our experimental resolution along three different azimuths ([010], [001] and [011]). This feature is reproduced much more accurately in TBHF + Σ calculations [9], where a peak is predicted at around 0.8 eV binding energy (referenced to the Fermi energy), which appears to be highly localized, showing a dispersion along ΓX of only around 0.3 eV. This feature originates in an antibonding combination of $d_{x^2-y^2}$ with the O 2p states, and is predicted to have strongly mixed Cu 3d and O 2p character [9]. We discuss the atomic character of this state as revealed by experiment in sections 3.1.4 and 3.2.

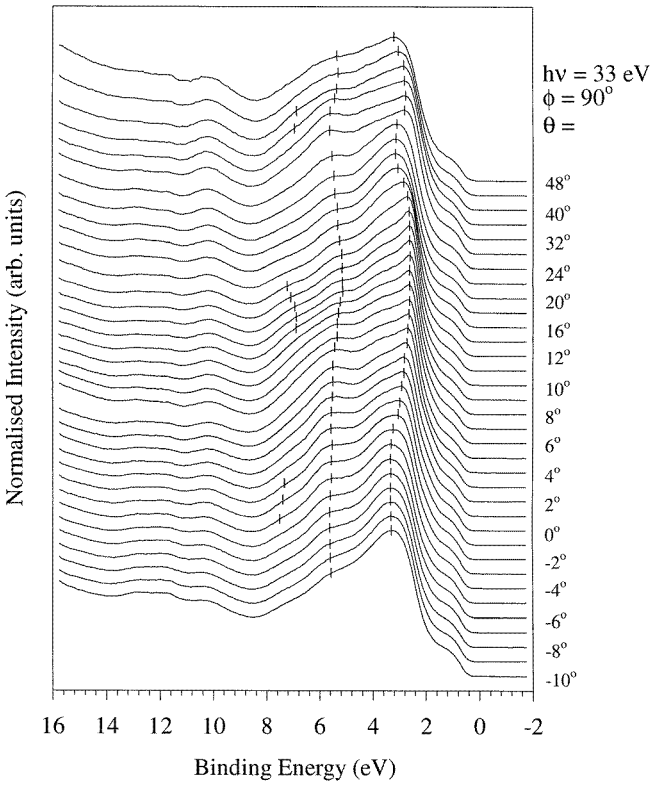

(a)

Figure 4. (a) Angle-resolved EDC spectra recorded using 33 eV photon energy along the c^* direction. Spectra have been normalized to the valence band intensity maximum. Photoelectron emission angles relative to the surface normal (θ) and the b^* axis of the crystal BZ (ϕ) are shown. (b) The 3D plot through the Brillouin zone traced out by the valence band intensity maximum of the spectra in figure 4(a). The sizes of the points represents the experimental error, and the point at $\theta = -10^\circ$ is tagged with a black circle. The calculation of the $k_\perp$ component uses values of $m^* = 0.95m_e$ and $V = 8$ eV (see text). (c) The experimental dispersion of the valence band intensity maximum (∼3 eV BE) and the bands at ∼5.5 eV and ∼7 eV along the ΓA direction, mapped onto the OLCAO bandstructure calculation of [7]. No adjustment of binding energy scale has been made between the calculated and experimental data.

Simple LDA calculation cannot reproduce the satellite structure at 9–13 eV [7, 9]. The latter anomaly has been noted by Ghijsen *et al* [4], who observe that while one-electron band structure calculations appear adequate for Cu_2O, for CuO the electron correlation effects in the open d-shell bands lead to the appearance of satellite structure not reproduced in such calculations. More recent calculations which aim to modify LDA results by introducing correlation more explicitly have reproduced satellite structure with varying degrees of success. The structure appears in both SIC − LSD and LSD + U approaches, but shifted to lower binding energy than observed experimentally [8]. It is not reproduced accurately in TBHF spectral functions, but is given moderately well in terms of both energy and relative intensity in TBHF + Σ results [9].

The general features of the spectra (valence band width, absence of Fermi level crossing, strongly localized feature at the top of the valence band and satellite structure in

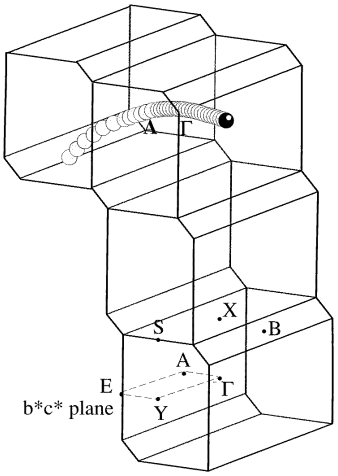

(b)

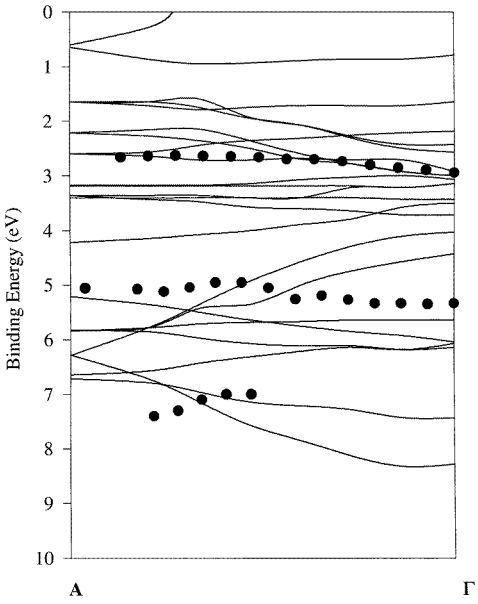

(c)

Figure 4. (Continued)

the range 9–13 eV) are reasonably well reproduced by the TBHF + Σ spectral functions [9]. We explore below the extent to which we can make a more detailed comparison of the experimental dispersions with this momentum-resolved calculation, and with simple LDA.

3.1.2. Preliminary considerations. For more thorough comparison, the path of each experimental measurement through the 3D Brillouin zone has been calculated by relating the kinetic energy and direction of the emitted photoelectron to the $\boldsymbol{k}$ vector of the electron within the crystal. Electron momentum is conserved parallel to the crystal surface, making

calculation of $\boldsymbol{k}_{\parallel}$ trivial; but certain assumptions are necessary in order to calculate the perpendicular component $\boldsymbol{k}_{\perp}$. Here we have used the 'direct transition' method, which assumes that conservation of momentum holds along the surface normal [17]. Due to the presence of the surface, the calculation of the perpendicular component is subject to assumptions concerning the electron effective mass and the surface barrier potential. This has the result that for the CuO(100) face, the electron momentum in the (100) plane may be specified accurately, with the projection perpendicular to this (along ΓX) affected by the values of m^* and V (the potential barrier at the surface) chosen. V was assumed to be 8 eV [17], and the effective electron mass value m^* chosen was $0.95m_e$. This was chosen, in the absence of other information, to be that used for NiO [18]. An alternative approach, the 'non-direct transition' method, assumes conservation of momentum holds parallel to the surface, but not perpendicular to it (i.e the resulting photoemission spectra are effectively angle integrated in the direction perpendicular to the surface) [19]. In fact, these two possible approaches are limiting cases, with the behaviour of most samples falling somewhere in between, depending on the photoelectron lifetime [20]. The extent of $\boldsymbol{k}_{\perp}$ conservation may be tested by recording photoemission spectra at normal emission as a function of photon energy; in this geometry, only the perpendicular component of the electron momentum is varied, and if there is no conservation of $\boldsymbol{k}_{\perp}$, no dispersion should be observed. Data taken in this geometry are discussed in section 3.1.4; for the present purposes, we merely note these show similar dispersions to those observed in other geometries, lending credence to our use of the 'direct transition' model here.

The comparison between calculated band structure and photoemission data is in principle a very delicate matter. Firstly, the intensities of photoemission data are strongly influenced by the photoionization cross sections of the atomic sublevels giving rise to the signal. This can make comparison with calculated total densities of states functions difficult. For the majority of the measurements shown here, the photon energy used (33 eV) was chosen such that the Cu 3d and O 2p photoionization cross sections are very closely matched [21], making comparison of calculated and experimental intensities more straightforward. In addition, photoemission data represent one electron removal spectra, whereas some calculations (for example the simple LDA calculations [7]) are representative of the ground state of the system. For this reason, direct comparison with these calculations must be treated with caution. However, in more recent calculations (LSD + U, SIC − LSD, TBHF + Σ), the use of the three particle approximation for the excited states has allowed the extraction of a calculated spectral function [8, 9], facilitating direct comparison with experiment. To date, momentum-resolved spectral functions are available only for the ΓX, ΓY and ΓZ directions, from TBHF + Σ [9]. In the discussion below, we have compared our data with these calculations where possible, and, failing that, with LDA where available [7].

3.1.3. Data collected along [001] and [010] azimuths. The 3D projection of the path traced in the Brillouin zone is shown together with the appropriate valence band EDCs for each experiment. Figure 4(a) shows valence band spectra recorded at 33 eV photon energy along the c^* axis ([001] azimuth) as a function of analyser position (from $\theta = -10^\circ$ to +48°). The features on the higher binding energy side of the valence band (around 5–6 eV binding energy) show some dispersion, with an additional feature appearing for certain analyser angles at around 7 eV. The intensity maximum of the valence band at 3 eV shows a small amount of dispersion of perhaps 0.7 eV. No density of states is observed at the Fermi edge and there is no discernible movement (at our experimental resolution) in the feature at around 1 eV binding energy. The experimental trajectory shown in figure 4(b) passes through two Brillouin zones with $\theta = 0^\circ$ corresponding to Γ and $\theta \approx 12$–16° to point A. The path ΓA along c^* is closely followed, but at larger polar angles the path curves away from this axis.

There is some qualitative agreement with the simple LDA band structure calculation over the ΓA region (figure 4(c) [7]). This shows densely packed, rather flat bands in the upper part of the valence band (1.5–3.5 eV binding energy), showing a maximum dispersion of around 1 eV. More strongly dispersing bands are seen at higher binding energies (around 5–8 eV). This comparison must of course be treated with caution, as the band structure represents the bulk ground state of CuO, and our experiments reflect the JDOS of initial and final states. Nevertheless, the LDA DOS functions show positions of maximum density of states predicted to lie at around 3 eV and 6 eV below E_F, with a smaller feature at around 7 eV [7]. These energies are in good agreement with the binding energy positions of the most intense bands of the experimental photoemission, which are plotted over the calculated bandstructure in figure 4(c).

Figure 5(a) shows the valence band dispersion over the same polar angle range and azimuth, using 45 eV photon energy. Again, there is very little dispersion of the valence band maximum, but the features to higher binding energy show more significant changes. From $\theta = -10^\circ$ to 0° a feature around 5 eV seems to move to higher energy and diminish, and a feature at 7–8 eV appears around $\theta = 28^\circ$ to 48°. Figure 5(b) plots the 3D path for this valence band dispersion, showing the path through two Brillouin zones, travelling along XB. X is at approximately $\theta = 0^\circ$ and B is close to $\theta = 12^\circ$. The theoretical band dispersion has not been calculated over this region.

Figure 6(a) shows the valence band spectra over the same polar angle range, but along a different azimuth. These data were recorded at 33 eV photon energy and follow the b^* direction ([010] azimuth). They show the now familiar pattern of dispersion: relatively small changes in the valence band maximum position, but some more complex splitting of bands in the 5–8 eV region. The experimental trajectory (figure 6(b)) describes a path essentially along ΓY (from $\theta = 0^\circ$ to 12–16°) which then curves through the second Brillouin zone. Figure 6(c) shows the positions of the two main intensity maxima of the experimental valence band overlaid on the LDA calculation for the ΓY direction. Again, the binding energy positions of the two intensity maxima match well with the calculated binding energies of maxima in the DOS [7]. The dispersion of these two most intense bands is very slight; however the calculated bands in these energy ranges also show very flat dispersion (figure 6(c)).

For this direction, a momentum-resolved spectral function is available from TBHF + Σ calculation [9], which is compared with our data in figure 6(d). In order to make this comparison, the calculated data have been shifted to higher binding energy by 0.4 eV to account for a difference in zero energy point; our data are referenced to the Fermi energy, while the zero of the calculated spectral function was originally set at the top of the valence band [9]. The calculation shows three main features; a set of mainly Cu 3d-related features peaking at around 3 eV binding energy, some weaker, mostly O 2p bands at around 5 eV and the feature discussed earlier at around 0.8 eV. None of these features show strong dispersion along ΓY, and their binding energies are in broad overall agreement with the experimental data. However the fine structure evident in the calculated data, and the changes in it between Γ and Y are not evident in the experimental spectra, which show very flat band behaviour across this range. This is partly attributable to the difference in resolution between calculated and experimental data. Our combined (monochromator + analyser) resolution is 0.16 eV, and the data are additionally recorded at room temperature. These two factors make it difficult to discern fine structure occurring on an energy scale less than around 0.3 eV, and so it is possible that more fine detail might emerge from an experiment undertaken at higher resolution. However, even taking this into account, it appears that the experimental features are intrinsically broader than the calculated ones. This may be attributable to the neglect of lifetime broadening in the calculation [9].

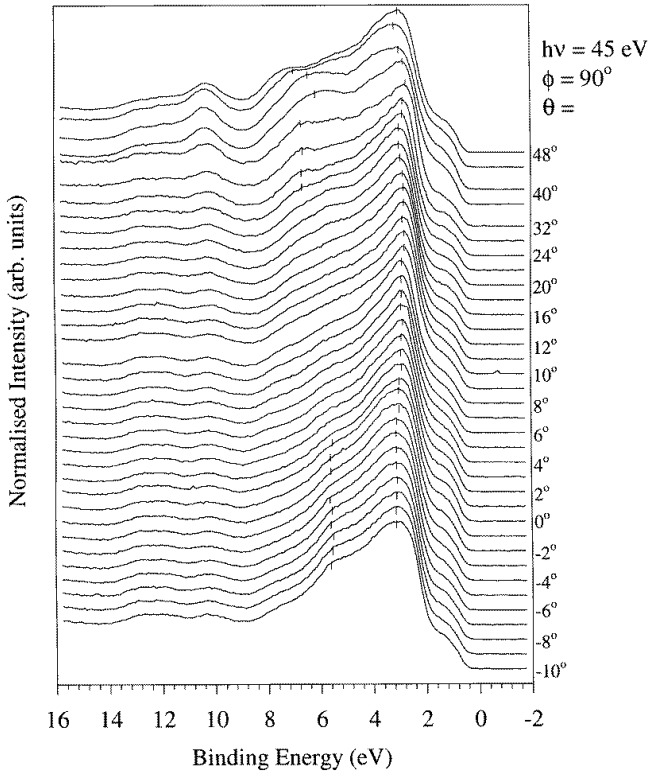

(a)

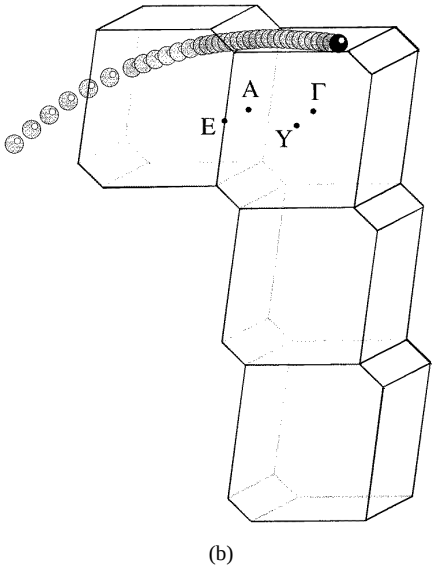

(b)

Figure 5. (a) Angle-resolved EDC spectra recorded using 45 eV photon energy along the c^* direction. Spectra have been normalized to the valence band intensity maximum. Photoelectron emission angles θ and ϕ are labelled as for figure 4(a). (b) The 3D plot through the Brillouin zone traced out by the valence band intensity maximum of the spectra in figure 5(a). The size of the points represents the experimental error, and the point at $\theta = -10^\circ$ is tagged with a black circle. The calculation of the $k_\perp$ component uses values of $m^* = 0.95m_e$ and $V = 8$ eV (see text).

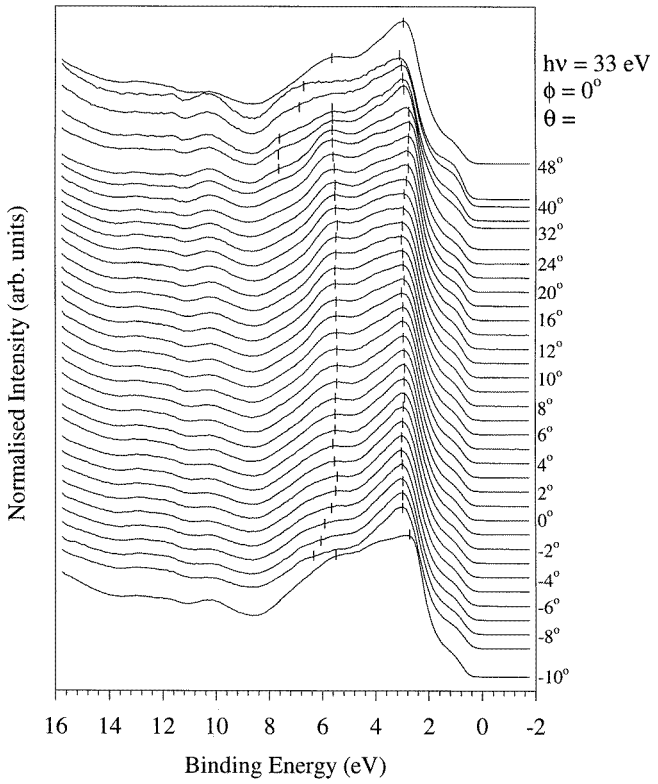

(a)

Figure 6. (a) Angle-resolved EDC spectra recorded using 33 eV photon energy along the b^* direction. Spectra have been normalized to the valence band intensity maximum. Photoelectron emission angles θ and ϕ are labelled as for figure 4(a). (b) The 3D plot through the Brillouin zone traced out by the valence band intensity maximum of the spectra in figure 6(a). The size of the points represents the experimental error, and the point at $\theta = -10^\circ$ is tagged with a black circle. The calculation of the $k_\perp$ component uses values of $m^* = 0.95m_e$ and $V = 8$ eV (see text). (c) The experimental dispersion of the valence band intensity maximum ($\sim$3 eV BE) and the band at $\sim$5.5 eV along the ΓY direction, mapped onto the OLCAO bandstructure calculation of [7]. No adjustment of binding energy scale has been made between the calculated and experimental data. (d) A comparison of the experimental data for the ΓY direction (lower panel) with the spectral functions for this direction calculated by TBHF + Σ [9] (upper panel). The spectra are referenced to the experimentally determined Fermi energy (see text), requiring a shift in the calculated data of 0.4 eV to higher binding energy. A simple linear background has been subtracted from the experimental data to facilitate comparison.

The effect of photon energy on this data set is shown in figure 7(a), which shows the valence band dispersion over the same polar angle range and azimuth, using 45 eV photon energy. Again, there is very little dispersion of the valence band maximum, but the features to higher binding energy show more significant variations. From $\theta = -10^\circ$ to 0° a feature around 7 eV seems to disappear, and reappear around $\theta = 28^\circ$ to 48°. The corresponding path through the Brillouin zone (figure 7(b)), for data recorded using this higher photon energy, is parallel to the path for data recorded at 33 eV (figure 6(b)). These data describe a path along XS, rather than through the centre of the first Brillouin zone, which then curves downwards. X corresponds to $\theta = 0^\circ$ and S to approximately $\theta = 16^\circ$. The LDA band structure over this

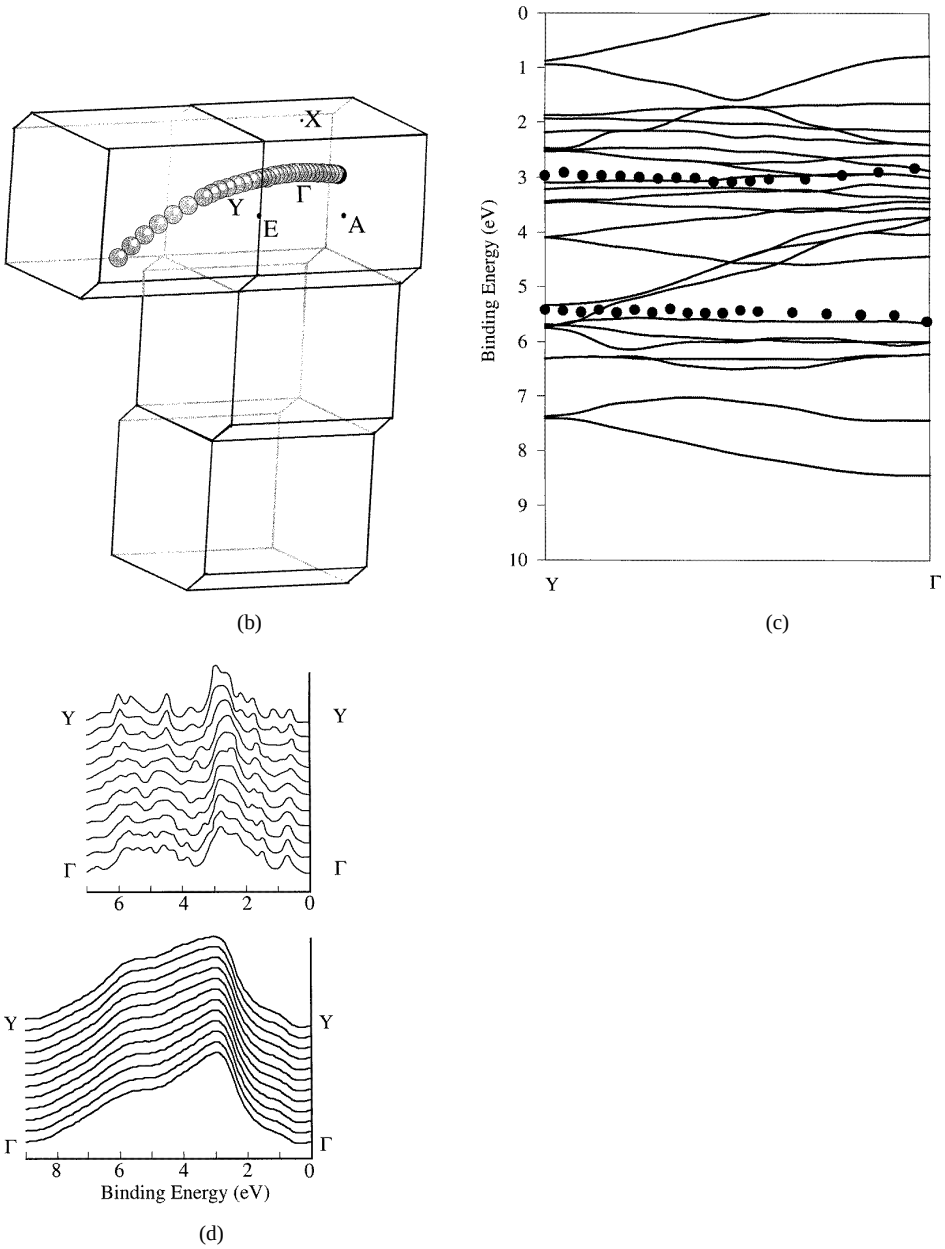

Figure 6. (Continued)

region shows no dispersion of the valence band maximum, but some splitting of bands in the 5–8 eV binding energy region between X and S [7].

3.1.4. Data collected in normal emission geometry. The dispersion of the valence band states has also been measured for the direction perpendicular to the b^*c^* plane, along ΓX. This is achieved by varying the energy of the incident photons, and keeping the analyser

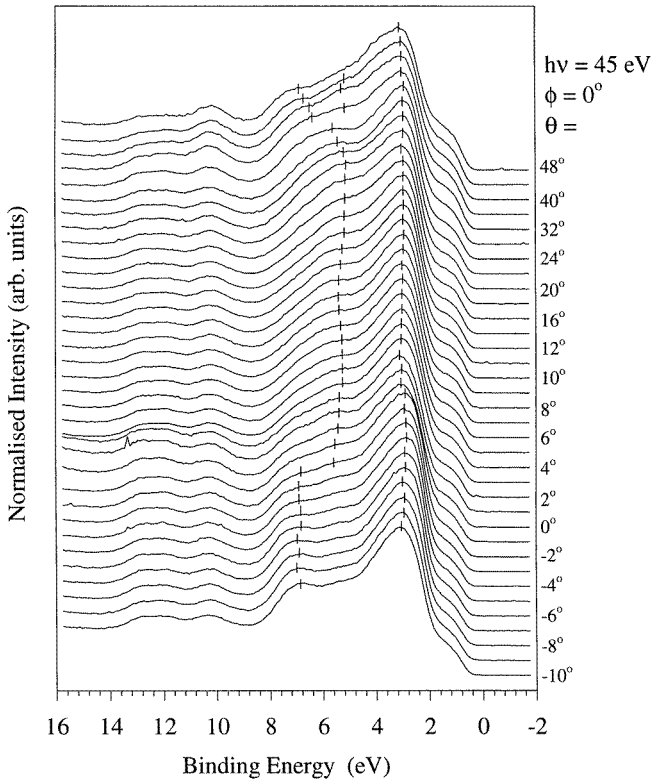

(a)

Figure 7. (a) Angle-resolved EDC spectra recorded using 45 eV photon energy along the b^* direction. Spectra have been normalized to the valence band intensity maximum. Photoelectron emission angles θ and ϕ are labelled as for figure 4(a). (b) The 3D plot through the Brillouin zone traced out by the valence band intensity maximum of the spectra in figure 7(a). The size of the points represents the experimental error, and the point at $\theta = -10^\circ$ is tagged with a black circle. The calculation of the $k_\perp$ component uses values of $m^* = 0.95m_e$ and $V = 8$ eV (see text).

position fixed to detect photoelectrons emitted perpendicular to the surface. This is shown in figure 8(a) for the photon range 24 to 70 eV, measured at normal emission, $\theta = 0^\circ$. To high binding energy, the spectra are dominated by the increasing secondary electron tail which appears at low photon energies. The valence band intensity maximum shows little dispersion, but the feature to the low binding energy side (around 1 eV binding energy) shows an increase in intensity relative to this as the photon energy increases, and the high binding energy features show some splitting and dispersion. In this geometry, only the perpendicular component of the electron momentum, $k_\perp$, is varied, so that the observation of dispersion along this azimuth supports our use of the 'direct transition' model [17] in analysis of the angle-resolved data. Figure 8(b) displays the experimental trajectory calculated using the assumed values for m^* (effective electron mass) and V (barrier potential) as explained above. Because of the monoclinic symmetry of the system, the points follow a line at an angle of 9° from the a^* axis. This line is close to $\Gamma_1 X \Gamma_2$, starting at Γ_1 (at 28 eV), reaching X at around 42 eV, with Γ_2 close to the position at 65 eV. The valence band spectra show similarities on passing through the two nearly equivalent points close to Γ. In particular, we note that spectra taken with photon energies 28–30 eV and 60–70 eV are characterized by two high binding energy

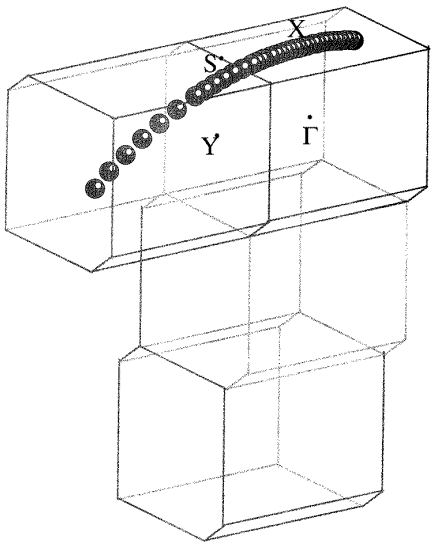

(b)

Figure 7. (Continued)

features in the binding energy range 6–8 eV (whereas only one is seen at intermediate photon energies). However, the relative intensities of the valence band features are not the same at Γ_1 as close to Γ_2. There is a decrease in relative intensity in the features between 5 eV and 8 eV binding energy with increasing photon energy. One reason for this is the change in background between 28 eV and 65 eV spectra, which contributes to the intensity of the high binding energy features in the 28 eV spectrum. The change in relative intensities in the valence band is nevertheless still evident in figure 8(c), where a simple linear background has been subtracted from the data. In the range 0–3 eV binding energy, where background effects are minimal, it is clear that there is an increase in the intensity of the feature at 1 eV BE relative to the valence band intensity maximum at 3 eV BE (figure 8(a)). Unlike our other experiments, in order to probe this azimuth normal to the surface, the photon energy is varied, which means that the photoionization cross-sections of the Cu 3d and O 2p states are not constant during the measurement. This will contribute to changes of relative intensity of the valence band states over the photon energy range, hampering comparison with calculation. The ratio of cross-sections O 2p/Cu 3d diminishes as the photon energy increases; at 28 eV this ratio is around 1.1, while at 65 eV it has fallen to only around 0.4 [21]. Differences between spectra recorded at different photon energies, but originating from the same point within the BZ, may therefore give us some information about the atomic parentage of the valence band states. The 28 eV photon energy spectrum provides a good representation of the O 2p and Cu 3d JDOS (as the ratio of cross-sections is roughly unity), whereas in the 65 eV spectrum the Cu 3d contribution is dominant. This would suggest that the states at 1 eV show less O 2p (and consequently more Cu character) than the valence band intensity maximum. We note that the feature at around 1 eV binding energy is quite strong in the Al Kα XPS of single crystal CuO [12]; as the O 2p/Cu 3d cross section ratio at this photon energy is only 0.02 [21], this is an indication of some substantial Cu 3d character in this part of the DOS function.

The momentum-resolved spectral function has been calculated by TBHF + Σ for this azimuth, and the comparison with our data is shown in figure 8(c) [9]. As for the ΓY direction,

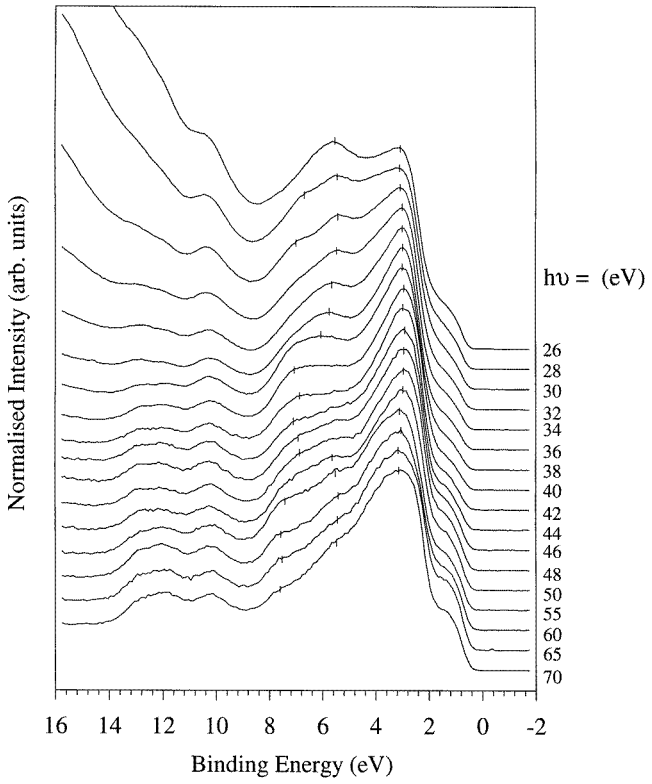

(a)

Figure 8. (a) Angle-resolved EDC spectra recorded using photon energies from 26 to 70 eV. The spectra are normalized to the valence band intensity maximum. All spectra were recorded at normal emission. This corresponds with a path through k-space perpendicular to the b^*c^* plane. (b) The 3D plot through the Brillouin zone traced out by the valence band intensity maximum of the spectra in figure 8(a). The size of the points represents the experimental error, and the point at $h\nu = 24$ eV is tagged with a black circle. The calculation of the $k_\perp$ component uses values of $m^* = 0.95m_e$ and $V = 8$ eV (see text). There is no $k_\parallel$ component of electron momentum for this experimental geometry. (c) A comparison of the experimental data for the ΓX direction (lower panel) with the spectral functions for this direction calculated by TBHF + Σ [9] (upper panel). The spectra are referenced to the experimentally determined Fermi energy (see text), requiring a shift in the calculated data of 0.4 eV to higher binding energy. A simple linear background has been subtracted from the experimental data to facilitate comparison.

there is a reasonable correspondence of the main features in terms of binding energy. Our observation of a decrease in relative intensity of the features between 5 eV and 8 eV binding energy with increasing photon energy is consistent with the strong O 2p character of the states predicted by the calculation in this range. Between Γ and X, the calculations show some dispersion of these features to higher binding energy, which is generally replicated in the experimental data, although our data show states tailing to higher binding energy than predicted (again, possibly attributable to the neglect of lifetime broadening in the calculation [9]). However, the splitting of the main Cu 3d part of the valence band predicted at X is not replicated in our data, and, at our experimental resolution, we do not resolve the splitting of the 1 eV feature predicted at this point. However, we note that the calculations predict substantial Cu 3d character for this feature, which is consistent with our observation that it remains strong

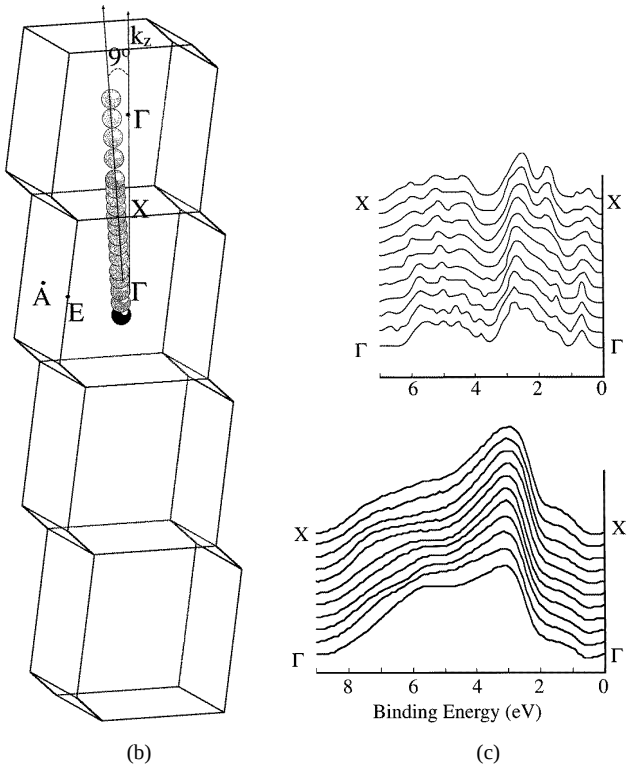

(b) (c)

Figure 8. (Continued)

at high photon energy. The atomic character of this part of the spectral function is discussed further in the light of resonance photoemission data presented below.

3.2. Cu 3p resonant photoemission; comparison with CI calculations

3.2.1. General comparison. The nature of the Cu 3d contributions to the main valence band is conveniently examined using Cu 3p resonant photoemission. Figure 9 shows stacked EDC spectra recorded over the photon energy range $h\nu = 70$ to 80 eV, passing through the Cu 3p $\rightarrow$ Cu 3d threshold at 74 eV. The increase in intensity in the satellite region at this threshold value is particularly marked for the part of the satellite feature at around 12 eV. The valence band in contrast shows little change over this energy range. This matches the results of Ghijsen *et al* from oxidized copper foils [5].

Figure 11 shows the CIS (constant initial state) scans recorded from the cleaved CuO crystal. The binding energy positions used are those labelled in figure 10. All the data are shown normalized to the beam monitor and are shown relative to the same vertical scale. The main valence band appears to show weak antiresonance, and the satellite features show resonance at the Cu 3p $\rightarrow$ Cu 3d threshold where $h\nu = 74$ eV. The largest resonant enhancement is for the satellite feature at 11.85 eV. Theoretical calculations of the resonance behaviour [4] (discussed further in section 3.2.2) predict a very strong enhancement in this binding energy range. The two peaks seen in the resonance signal are separated by approximately 2.3 eV. This value is the spin–orbit splitting of the Cu $3p_{3/2}$ and $3p_{1/2}$ orbitals, and indicates both these levels are involved in the resonance process [5, 22].

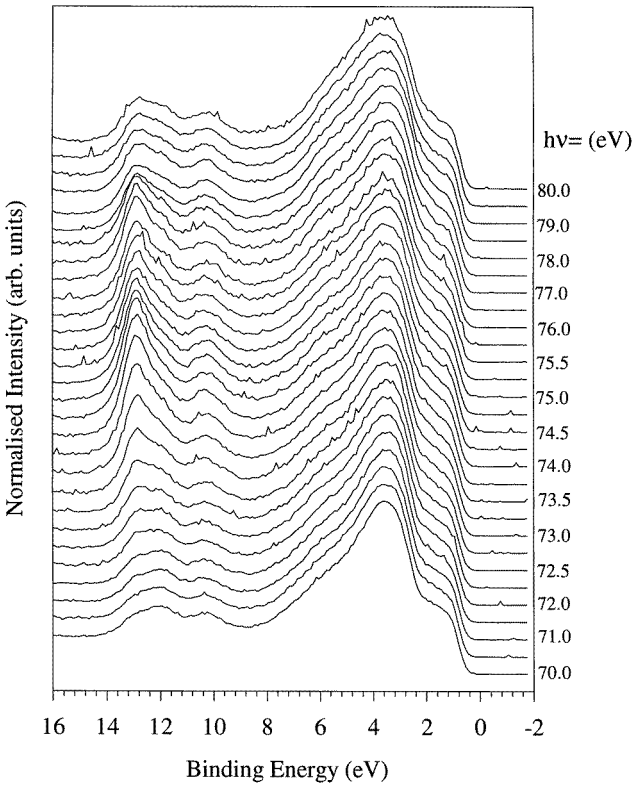

Figure 9. Valence band EDC spectra as a function of photon energy, passing through the Cu 3p → 3d resonance at $h\nu = 74$ eV. The spectra are normalized to the valence band intensity maximum.

The normal photoemission process is:

$$3p^6 3d^n + h\nu \rightarrow 3p^6 3d^{n-1} + e^-.$$

At resonance, this is augmented by a Coster–Kronig intra-atomic decay which may be described as:

$$3p^6 3d^n + h\nu \rightarrow \{3p^5 3d^{n+1}\}^* \rightarrow 3p^6 3d^{n-1} + e^-.$$

The resonance process emphasizes the local character of the states [9]. Thus, as CI calculation treats the electron correlations within the cluster exactly, it provides a good description of the observed resonances. These calculations describe the main valence band final state composition as $d^9\underline{L}$ (i.e. screened final state) with the complex satellite structure arising largely from unscreened d^8 states (in the range 9–13 eV binding energy), and some $d^{10}\underline{L}^2$ states lying at around 9–10 eV binding energy [6]. The small satellite at around 16.5 eV binding energy has unscreened d^8 character [6]. The resonance process above may only produce d^8 final states, which will show a strong Fano type resonance at the appropriate photon energy; thus the observation of strong resonance for the satellite features is consistent with their unscreened character, while the resonance behaviour of the main valence band is expected to be less marked. Approximating the local coordination of Cu in CuO to square planar (D_{4h}), Ghijsen *et al* have calculated the d^8 singlet and triplet spectral profiles [5]. The singlet satellite features are calculated to show the strongest resonance effect. This is mainly due to the presence of a

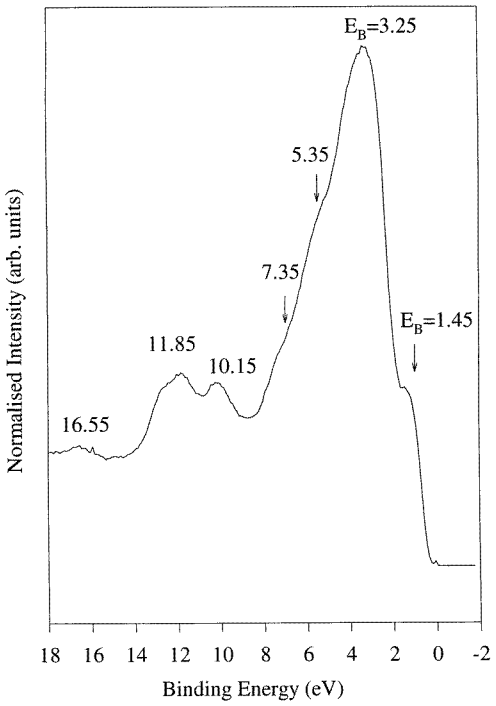

Figure 10. A typical valence band EDC spectrum recorded at 70 eV photon energy. The labelled positions indicate the binding energies at which CIS resonance experiments were carried out (figure 11).

^{1}G final state with binding energy of ≈12.5 eV, which has a significantly higher Auger decay matrix element than the triplet states at ≈10 eV binding energy. The net effect is that whilst the main satellite feature spans the range 10–13 eV binding energy, the strongest resonant enhancement is expected at around 12 eV binding energy, as observed here.

For compounds in which the screened final state may be accessed directly from the resonating state (e.g. Ni^{II} oxides, where the initial d count is d^8), valence band antiresonance has been observed (and, in the case of Ni, assigned to screened $3d^8\underline{L}^1$ final states [23]). As described earlier, any resonant effect from $d^9\underline{L}^1$ states in the case of Cu^{II} oxides is expected to be weaker than the effects observed in the corresponding Ni oxides. We thus assign the observation of weak Fano antiresonance in the main valence band to $d^9\underline{L}$ final states. Our results therefore show the satellites to be predominantly d^8 character, and the main valence band to be $d^9\underline{L}$, in excellent agreement with the CI calculations. This behaviour is almost identical to that seen for both oxidized copper films [5], and for composites of small CuO crystals [12]. However, the small satellite at 16.5 eV shows a weak resonant effect, in contrast to previous experiments on composites of single crystals of CuO where this feature showed antiresonant behaviour [12]. This feature is observed in the Al Kα spectrum of single crystal CuO [12], and is predicted by CI calculations, which show it to be part of the d^8 singlet DOS, of $^1A_{1g}$ symmetry [5, 6] (within the approximation of D_{4h} symmetry used in the calculation; ^1A_g within the actual C_{2h} local point group symmetry at the Cu sites). The resonance behaviour seen here is fully consistent with these calculations, and with data from oxidized films [5, 24], which indicate that this feature is expected to show resonant, rather than antiresonant, behaviour. We tentatively suggest that this small feature could be hidden in measurements with a high

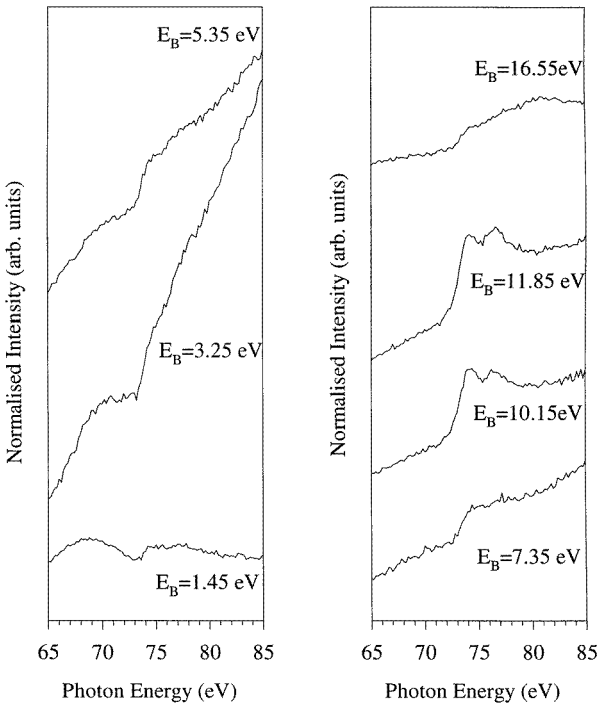

Figure 11. CIS scans across the Cu 3p → 3d threshold at ∼74 eV at the binding energy positions labelled in figure 10. The spectra are normalized to the incident beam monitor reading. The tungsten absorption coefficient of the beam monitor is featureless in this photon energy range.

secondary electron background, and the smooth surface generated here by cleaving a large single crystal may favour its detection.

3.2.2. Direct comparison with CI calculations. In figure 12, we make a more explicit comparison with calculated data by plotting our CIS spectra on the same scale as the calculations of Ghijsen *et al* [5]. In order to make this comparison, we have first subtracted a linear background from each experimental spectrum. (The valence band data in particular have steeply rising backgrounds; these tend to be most evident in CIS from sharp maxima, such as the valence band maximum at 3.25 eV, and can arise from small errors in monochromator positioning during the data accumulation). The positions chosen for our CIS measurements correspond to intensity maxima in the experimental spectrum, and are at slightly different binding energies from those used in the calculation. Some approximations are therefore necessary in making the comparison. We have chosen to scale the minimum–maximum height of the largest observed resonance (the satellite feature at 11.85 eV binding energy) to the corresponding calculated satellite feature (12.7 eV [5]). The abscissa for the calculated data is chosen by aligning the binding energy positions of the maxima of these two resonances. The remaining data are presented relative to these scales. In general, it can be seen that the agreement between calculated and experimental spectra is very good, both in terms of the relative intensities of the resonances and their binding energy positions. The most serious discrepancy in intensity arises for the valence band maximum (3.25 eV binding energy), where the experimentally determined resonance appears to be substantially stronger than the calculated one (binding energy 3.5 eV). This may suggest that the copper character of this

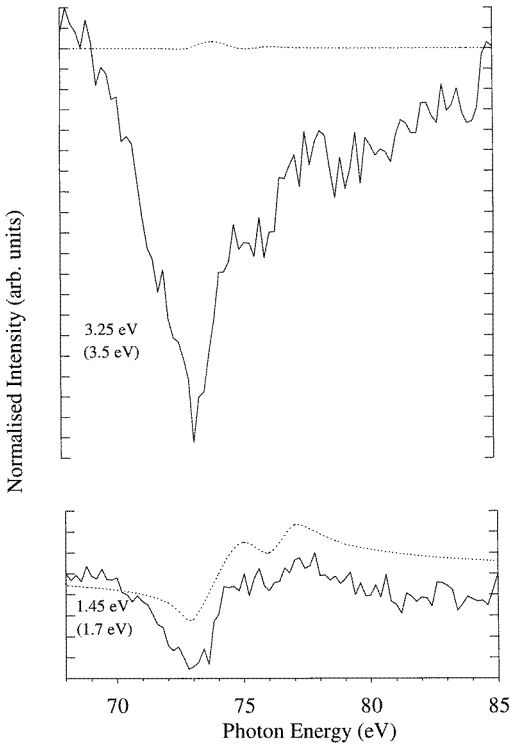

Figure 12. Comparison of experimental CIS data (solid lines) with the calculated resonance profiles of Ghijsen *et al* [5] (dotted lines). The data are aligned and scaled relative to each other as described in the text, following subtraction of a linear background from the experimental data. The experimental binding energy positions (as selected in figure 10) are shown; the binding energies shown in parentheses indicate those used in the calculation of the corresponding resonance profile [5].

part of the valence band is stronger than predicted by the cluster calculations. However, we note that the initial spectrum in this case was superimposed on a very steep rising background (figure 11), and any inaccuracies in background subtraction will have a marked influence on the apparent strength of this feature. It would therefore be unwise to draw conclusions from this apparent anomaly.

In general, the binding energy positions and shapes of the resonances agree well. In particular we note that the experiment, like the calculation, shows an antiresonance dip with a significantly delayed resonance onset for the feature at 1.45 eV binding energy (1.7 eV binding energy in the calculation). In the cluster calculations, this feature arises from a singlet state of ^1A_g symmetry ($^1A_{1g}$ within the D_{4h} approximation of the calculation), which is primarily a $d^9\underline{L}^1$ final state, with one hole in a $d_{x^2-y^2}$ orbital, and the other in an O 2p orbital [4, 6]. It is predicted to have only a few per cent unscreened d^8 character [4]. Strong evidence for the presence of this so-called 'Zhang–Rice' singlet has recently emerged from elegant spin-resolved experiments [14]. Our results appear to be in good agreement with the screened nature of this state predicted by CI calculations [5]. At first sight, this observation appears to be contrary to the results of our normal emission measurements, where cross-section arguments indicate appreciable Cu character in these states. A similar phenomenon has been observed by

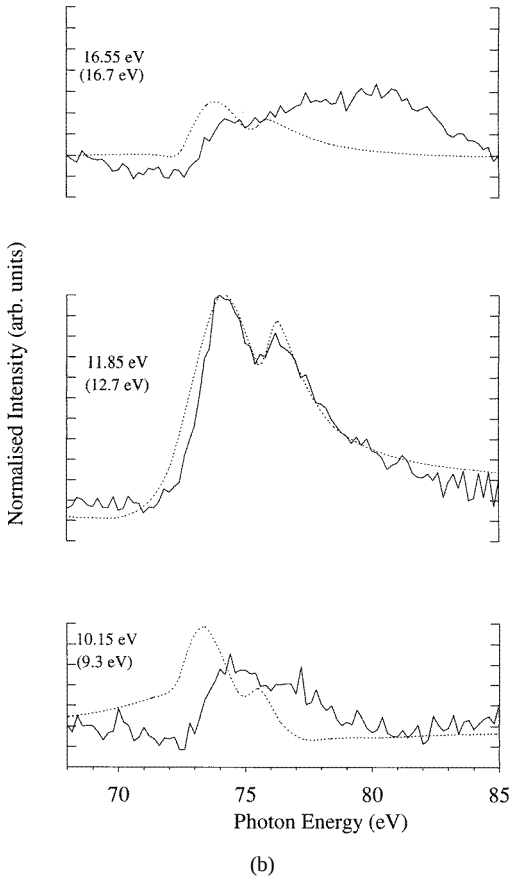

(b)

Figure 12. (Continued)

List *et al* in superconducting cuprates. Using cross-section arguments, these authors arrived at a figure of 35% Cu 3d character for the Zhang–Rice singlet in the related cuprate superconductor $Bi_2Sr_2CaCu_2O_8$, again in apparent disagreement with the very weak antiresonance observed in their own Cu 3p resonant photoemission [25]. We note that TBHF + Σ calculations reproduce the essentially localized nature of this feature, but show it to have strongly mixed Cu 3d and O 2p character [9]. Thus we conclude that while giving clear information about the screened nature of the final state, resonant photoemission within the main valence band of Cu^{II} compounds may not be a particularly safe guide to the degree of Cu character of the *initial* state as the $d^9\underline{L}^1$ final state is not directly accessible via the resonating state, resulting, as we have seen, in very weak effects across the binding energy range 1–8 eV [25, 26]. The appreciable Cu character in this part of the spectral profile indicates that CuO is somewhat different to a conventional charge-transfer insulator.

In terms of binding energy position, the most serious discrepancy between experiment and calculation arises for the resonance at 10.15 eV binding energy (9.3 eV in the calculation). The calculated resonance shows an onset ahead of the strongest satellite resonance, while our data show a very slightly delayed resonance relative to the strongest feature at 11.85 eV. We note that while this part of the DOS profile is made up primarily of d^8 final states, $d^{10}\underline{L}^2$ states are also present [6], which may contribute to the slight resonance onset delay.

4. Conclusions

We have presented angle-resolved photoemission studies of an oriented copper oxide single crystal, and mapped these onto the 3D Brillouin zone of the monoclinic material. Resonant photoemission has been used to probe the atomic character of the spectral features. Comparison has been made where possible with a number of calculations, including CI [5], LDA [7] and recent TBHF + Σ [9] results.

The agreement with LDA calculations is generally poor, although the overall width and intensity distribution within the main valence band is reasonably well reproduced [7]. These calculations on the whole predict larger dispersions of the experimental features than are observed experimentally, particularly close to the Fermi energy. The calculations overlook explicit electron–electron interaction effects, predicting a Fermi surface for semiconducting CuO, and completely failing to reproduce the observed satellite structure. Band theory also fails to describe correctly other related oxides such as NiO and CoO for very similar reasons [27–29].

In contrast, localized cluster calculations, such as CI, accurately predict the appearance of the satellite structure and its resonance behaviour (as the resonance process emphasizes the local character [9]). The resonant photoemission from the single crystal shows good agreement with these calculations, and with data from polycrystalline CuO and thin films [5, 6, 12]. Most notably the feature at 16.5 eV, which was the subject of some dispute, clearly shows resonance behaviour, indicating its unscreened d^8 character. States at around 1.5 eV binding energy show weak antiresonant behaviour, indicating the screened nature of the final state, $d^9\underline{L}^1$. However, CI calculations by their nature can give no momentum-resolved information for comparison with angle-resolved photoemission.

Recent attempts to bridge the gap between localized and delocalized descriptions appear to be meeting with some success, and in particular the spectral functions calculated by the TBHF + Σ approach [9] appear to replicate the most significant features of our data. Here we have been able to make explicit contact with calculations of the spectral function for the ΓX and ΓY directions. The calculation predicts a non-metallic ground state, as we observe, and a valence band width and intensity distribution roughly in accord with experiment. In addition, satellite structure is predicted, with strong Cu character, and at binding energies which are in reasonable agreement with experiment. In terms of atomic character of the main valence band states, these calculations predict strong Cu character at around 3 eV binding energy, and strong oxygen character in more highly dispersing bands at 5–8 eV binding energy. The latter observation is in good agreement with normal emission data taken as a function of photon energy, and is consistent with earlier measurements [4, 12]. In contrast with LDA, the calculations also predict a strongly localized feature at around 0.8 eV binding energy, identified as the Zhang–Rice singlet, with strong Cu and O character. The presence of strong Cu character in this part of the spectral function is consistent with our observation that this feature remains intense at high photon energies. This feature nevertheless shows only weak antiresonance in Cu resonant photoemission. By comparison with a similar anomaly noted in the case of the superconducting cuprates [25], we conclude that for Cu^{II} the initial state may contain more Cu character than suggested by the weak antiresonance arriving at the screened final state. The presence of appreciable Cu character in the filled states closest to the Fermi energy means that CuO is not a pure charge-transfer insulator in the strict sense, although it may be regarded as charge-transfer type [9].

Overall, recent *ab initio* calculations (TBHF + Σ, LDA + U, SIC − LSD [8, 9]) which treat many body effects using the three particle approximation [10, 11] appear to provide a useful starting point for comparison with momentum-resolved experiments from this highly correlated oxide.

Acknowledgments

This work was supported by EPSRC (UK). SW acknowledges financial support from National Power Plc.

References

[1] Asbrink S and Norrby L-J 1970 *Acta Crystallogr.* B **26** 8
[2] Gmelin E 1992 *Ind. J. Pure Appl. Phys.* **30** 596
[3] Shannon R D and Prewitt C T 1969 *Acta Crystallogr.* B **25** 925
[4] Ghijsen J, Tjeng L H, van Elp J, Eskes H, Westerink J, Sawatzky G A and Czyzyk M T 1988 *Phys. Rev.* B **38** 11 322
[5] Ghijsen J, Tjeng L H, Eskes H, Sawatzky G A and Johnson R L 1990 *Phys. Rev.* B **42** 2268
[6] Eskes H, Tjeng L H and Sawatzky G A 1990 *Phys. Rev.* B **41** 288
[7] Ching W Y, Xu Yong-Nian and Wong K W 1989 *Phys. Rev.* B **40** 7684
[8] Laegsgaard J and Svane A 1997 *Phys. Rev.* B **55** 4138
[9] Takahashi M and Igarashi J 1997 *Phys. Rev.* B **56** 12 818
[10] Igarashi J 1983 *J. Phys. Soc. Japan* **52** 2827
[11] Igarashi J 1985 *J. Phys. Soc. Japan* **54** 260
[12] Shen Z-X, List R S, Dessau D S, Parmigiani F, Arko A R, Bartlett R, Wells B O, Lindau I and Spicer W E 1990 *Phys. Rev.* B **42** 8081
[13] Thuler M R, Benbow R L and Hurych Z 1982 *Phys. Rev.* B **26** 669
[14] Tjeng L H, Sinkovic B, Brookes N B, Goedkoop J B, Hesper R, Pellegrin E, de Groot F M F, Altieri S, Hulbert S L, Shekel E and Sawatzky G A 1997 *Phys. Rev. Lett.* **78** 1126
[15] Warren S, Thomas A G, Hollingworth J, Flavell W R, Wincott P L, Prime A, Downes S and Chen Changkang 1997 *Surf. Sci.* **377–379** 256
[16] Wanklyn B M and Garrad B J 1983 *J. Mater. Sci.* **2** 285
[17] See e.g. Courths R and Hüfner S 1984 *Phys. Rep.* **112** 54
[18] Shen Z-X, List R S, Dessau D S, Wells B O, Jepsen O, Arko A J, Bartlett R, Shih C K, Parmigiani F, Huang J C and Lindberg P A P 1991 *Phys. Rev.* B **44** 3604
[19] See e.g. Grandke T, Ley L and Cardona M 1977 *Phys. Rev. Lett.* **38** 1033
[20] Grandke T, Ley L and Cardona M 1978 *Phys. Rev.* B **18** 3847
[21] Yeh J J and Lindau I 1985 *At. Data Nucl. Data Tables* **32** 1
[22] Thuler M R, Benbow R L and Hurych Z 1993 *Phys. Rev.* B **27** 2082
[23] See e.g. Eisaki H, Uchida S, Mizokawa T, Namatame H, Fujimori A, van Elp J, Kuiper P, Sawatzky G A, Hosoya S and Katayama-Yoshida H 1992 *Phys. Rev.* B **45** 12 513
[24] Tjeng L J, Chen C T, Ghijsen J, Rudolf P and Sette F 1991 *Phys. Rev. Lett.* **67** 501
[25] List R S, Arko A J, Bartlett R J, Olson C G, Yang A-B, Liu R, Gu C, Veal B W, Chang Y, Jiang P Z, Vandervoort K, Paulikas A P and Campuzano J C 1989 *Physica* C **159** 439
[26] Cohen O, Cummins T R, Georgiadis G C, Rastomjee C S, Potter F H, Egdell R G, Flavell W R, Law D S-L and Leonyuk L 1994 *Physica* C **222** 105
[27] Sawatzky G A and Allen J W 1984 *Phys. Rev. Lett.* **53** 2339
[28] Terakura K, Williams A R, Oguchi T and Kuebler J 1984 *Phys. Rev. Lett.* **52** 1830
[29] Terakura K, Oguchi T and Kuebler J 1984 *Phys. Rev.* B **30** 4734